Universidad de Valladolid

Faculty of Sciences

Condensed Matter Physics Department

Master Thesis

Master in Molecular Nanoscience and Nanotechnology

Local electric field enhancement at the heterojunction region of SiGe/Si axially heterostructured nanowires

Jose Luis Pura Ruiz

July 2016

Supervised by

Óscar Martínez Sacristán

Agradecimientos

Quisiera agradecer con estas palabras a toda la gente que de una u otra manera ha contribuido a que este trabajo salga adelante.

En primer lugar a mis directores, Óscar Martínez Sacristán y Juan Jiménez, por su inestimable trabajo a mi lado y todo lo que he aprendido de ellos.

También quisiera agradecer el apoyo de todos los compañeros del grupo Optronlab, todos aquellos que día a día me ayudan a seguir avanzando con sus valiosos consejos y fructíferas discusiones.

Gracias también al Dr. Tomás Rodríguez, Dr. Andrés Rodríguez, y Dr. Thierry Baron, por suministrarnos los nanohilos que se han analizado en este trabajo.

Este trabajo ha sido financiado por la Junta de Castilla y León (Proyecto VA293U13) y el Ministerio de Economía y Competitividad (MINECO ENE2014-56069-C4-4-R), así como el Ministerio de Educación, Cultura y Deporte a través de una beca del Programa de Formación del Profesorado Universitario (FPU14/00916).

0. Resumen en Español 5
Introducción 5
Resultados 5
Conclusiones 6
1. Abstract 7
2. Introduction 9
3. Objectives 13
4. State of the Art 15
4.1. Raman Spectroscopy 15
4.2. Carrier dynamics in semiconductor NWs 19
4.3. Finite Element Method 21
5. Experimental 29
5.1. Sample Preparation 29
5.2. Simple Heterojunction NWs 31
5.3. Double Heterojunction NWs 36
5.4. Chemical Passivation of the NWs Surface 41
6. Simulations 45
7. Conclusions and Future Work 49

0. Resumen en Español

Introducción

Los nanohilos (NWs) semiconductores están atrayendo una gran atención en los últimos años debido a sus excepcionales propiedades. En particular, hay un gran interés en el estudio de la interacción luz/NW, ya que sus singulares propiedades ópticas los convierten en los candidatos óptimos para futuros dispositivos nanofotónicos. La radiación electromagnética interacciona con los NWs de forma muy diferente, dependiendo principalmente del diámetro de los NWs, la longitud de onda de la luz incidente y el índice de refracción, tanto del NW como del medio que lo rodea. Estas propiedades ópticas tan singulares se han puesto de manifiesto en diferentes fenómenos físicos recientemente descubiertos, como el incremento de la fotocorriente en NWs de Ge, la amplificación de los fenómenos de dispersión, extinción y emisión de luz, o la generación de segundo armónico, entre otros.

Resultados

En este trabajo se presenta un nuevo fenómeno de amplificación del campo electromagnético en la zona de la heterounión de NWs con heterouniones axiales de SiGe/Si, cuando son iluminados por un haz láser. La distribución del campo electromagnético se detecta por espectroscopía micro Raman, revelando una amplificación de la señal Raman producida en la región de la heterounión. En concreto, para la señal Raman por unidad de volumen producida por la heterounión, se observa una amplificación de en torno a 10 veces con respecto a la señal de los segmentos homogéneos. La reproducibilidad de este efecto se ha corroborado realizando medidas sobre NWs con distinta estructura y composición, e incluso crecidos por diferentes grupos, obteniendo resultados equivalentes.

Para explorar la física detrás de este fenómeno se han resuelto las ecuaciones de Maxwell para la interacción luz/NW utilizando elementos finitos (FEM). Para ello se ha diseñado un modelo tridimensional del sistema en estudio, calculando la distribución del campo electromagnético en el interior del NW, y derivando la señal Raman que produciría dicha distribución. El modelo muestra una localización y amplificación del campo electromagnético en la zona de la unión; sin embargo, los valores teóricos no reproducen la amplificación observada experimentalmente, lo que

sugiere la existencia de un mecanismo más complejo que la simple interacción de la luz con un NW dieléctrico. En una versión mejorada del modelo se incluye el efecto de los portadores fotogenerados sobre la respuesta óptica del NW, consiguiendo una mayor amplificación y logrando reproducir los valores experimentales.

La presencia de estos portadores fotoinducidos se ha comprobado realizando medidas sobre NWs de Si cuya superficie ha sido modificada por ataque químico. La modificación de la estructura de la superficie induce un cambio en la dinámica de portadores, que se reflejaría en una variación de la señal Raman. Los resultados obtenidos reproducen de manera satisfactoria el comportamiento que preveía la teoría al considerar presencia de portadores fotogenerados.

Conclusiones

Se ha mostrado un nuevo efecto de amplificación en nanohilos con heterouniones axiales de SiGe/Si. La amplificación observada en la señal Raman de la heterounión es de en torno a 10 veces con respecto a los segmentos homogéneos. Este efecto ha sido estudiado a través de un modelo de elementos finitos, con el que se han llegado a obtener los valores de amplificación obtenidos experimentalmente. Para ello se ha considerado el efecto de los portadores libres sobre la distribución del campo electromagnético en el interior del nanohilo heteroestructurado.

Este nuevo efecto de amplificación abre un nuevo camino para la mejora de los procesos de *photon harvesting*, así como la optimización de dispositivos optoelectrónicos, como fotodetectores, sensores, células solares, etc.

1. Abstract

Semiconductor nanowires (NWs) have been widely investigated in the last years because of their unique properties. In particular, there is a great interest in the interaction between semiconductor NWs and light, as their optical properties make them the optimal candidates for nanophotonic devices.

This work presents a phenomenon concerning the electromagnetic field enhancement at the heterojunction region of axially heterostructured SiGe/Si NWs when illuminated by a focused laser beam. The electric field is sensed by micro Raman spectroscopy, which reveals the enhancement of the Raman signal arising from the heterojunction region; the Raman signal per unit volume increases nearly 10 times with respect to the nanowire homogeneous segments. The effect has been corroborated by measuring several NWs with different composition and structure. In order to explore the physical meaning of this phenomenon, a 3-dimensional solution of the Maxwell equations of the interaction between the focused laser beam and the nanowire was carried out by finite element method. A local enhancement of the electric field at the heterojunction was deduced; however, the magnitude of the electromagnetic field enhancement is lower than the experimental results, thus suggesting a more complex phenomenon than the simple laser/NW dielectric interaction. In a second step, the role of the photogenerated free carriers was also considered, showing that the electric field at the carrier depleted heterojunctions provides a further electromagnetic field enhancement. The presence of free carriers has been tested in homogeneous Si NWs by a chemical passivation of its surface, and the study of the consequent modification of the carrier dynamics.

The existence of this amplification effect promises a way to improve photon harvesting using axially heterostructured semiconductor NWs, and the optimization of light-sensitive devices as photodetectors, sensors, solar cells, etc.

2. Introduction

Semiconductor nanowires (NWs) are attracting a great deal of attention because of the increasing number of potential applications in a wide variety of fields such as medicine, light and gas sensors, optoelectronics, or energy generation (solar cells, thermoelectric cells, etc). All of these promising applications arise from the NWs unique properties.[1] In fact, most of these properties are a direct consequence of the NW confined dimension, the diameter, as compared to some characteristic lengths, e.g. exciton Bohr radius, phonon mean free path, wavelength of the incident electromagnetic waves, etc.[2] The reduced radial dimension, as well as the high aspect ratio, yield a substantial difference in the NWs properties as compared to the corresponding bulk material.[3,4] The relationship between the size and the properties provides a new way of tailoring the properties of these materials by simply controlling characteristics as diameter, length, composition or surface condition. This give us an essential tool to create new devices with new properties and features which are now either unavailable or very difficult to implement with bulk materials.

A wide range of semiconductor NWs have been investigated in recent years. Among this variety we can find the following groups:

- Group IV semiconductor NWs. These NWs are compatible with the CMOS technology (Complementary Metal-Oxide Semiconductor), which is the basic technology of current microelectronics. The most studied NWs in this group are Si NWs, however, Ge NWs are recently under exhaustive investigation. Ge can offer new expectations with respect to Si, such as higher electron and hole mobilities, and more pronounced quantum effects. Moreover, the possibility of making $Si_{1-x}Ge_x$ alloys allow us to create a material with properties that can vary continuously between those of Si and Ge.[5] The SiGe alloy also permits the fabrication of heterostructures, which are essential in the development of nanodevices.

- Group III-V semiconductor NWs (GaAs, InP, etc). The main advantage of this kind of semiconductors with respect to group IV is the high electron and hole mobilities, much higher than that of Si or Ge. It has been recently reported an efficiency of 13.8% in solar cells based on InP NWs,[6] which is a very exciting result concerning the expectations of the NWs working as photovoltaic devices.

- Group III-N semiconductor NWs (GaN, InN, etc). These semiconductors have really interesting properties, the most representative one is the high value of their band gap, but also the possibility of the band gap engineering by making use of their alloys. III-N compounds have additional advantages, as the high exciton binding energy, high chemical stability, biocompatibility, etc.

- Metal oxides semiconductor NWs. In this group we find semiconductor NWs with high values of the band gap, direct band gap, high exciton binding energy, and, above all, the ease of their manufacture and the high crystalline quality. Nowadays, the research concerning these NWs is centered in photovoltaic devices based on metal oxides NWs.

According to the possible applications of semiconductor NWs that have been presented, there is a great interest in the study of the interaction between semiconductor NWs and light. Moreover, their optical properties make them the optimal candidates for nanophotonic devices.[7,8] A broad range of unique optical properties of semiconductor NWs have been reported, e.g. waveguiding,[9] optical resonances,[5] antenna effects, among others.[10] All these effects emerge because light interacts with the NWs in different ways depending on the NW diameter, wavelength, and dielectric properties of the NW and the surrounding media. One of the most relevant properties concerning the light/NW interaction is the ability of NWs to enhance their optical absorption/scattering for certain resonant diameters, which are characterized by large local electric fields inside the NW.[11] The absorption/scattering resonances deal with different phenomena recently reported, including, among other, the enhanced photocurrent response of NWs,[10] enhanced elastic and inelastic light scattering by Si NWs,[12] light extinction,[13] light emission in different semiconductor NWs,[14,15] and second harmonic generation.[9]

Since the Raman intensity is proportional to the excitation light intensity and the sample scattering volume, the experimental study of the interaction of light with matter at the nanoscale can be carried out by its Raman response. This makes Raman spectroscopy an excellent probe for sensing the local electric field induced inside the NW under incident light. In addition, it is possible to take advantage of its capabilities as a powerful non-destructive technique for the characterization of the structure, composition, stress, thermal, electronic, and optical properties of semiconductor NWs.[5,16-20] It is worth noting that up to now the research interest about the light/NWs interaction has been focused mainly on homogeneous single NWs and/or core-shell

heterostructured NWs;[21] however, the response of axially heterostructured NWs to the electromagnetic waves is still unexplored. These kind of structures are attracting an increasing interest since heterojunctions are necessary for the development of semiconductor NW based devices.[22] In the junction of these NWs a jump in the complex refractive index due to the abrupt change of material is expected, which therefore may change the electromagnetic response of the NW. Besides, the HJ built-in potential, which can locally change the polarizability, the oscillator strength and the presence of free carriers, could also affect the electric field distribution inside the NW.

To further advance in this subject, we present in this work a study of the distribution of the electromagnetic field in axially heterostructured SiGe/Si NWs, paying special attention to the role of the HJ in the optical response of the NW. This is carried out experimentally by using its Raman response as a sensor of the local electric field, which is compared to the 3-dimensional solution of the Maxwell equations characterizing the laser/NW interaction by finite element methods (FEM).

References

1. Y. Cui and C.M. Lieber. *Science* **291,** 851-853 (2001)

2. R. Rurali. *Rev. Mod. Phys.* **82**(1), 427-449 (2010)

3. M. Law. *Annu. Rev. Mater. Res.* **34**, 83 (2004)

4. R. N. Musin and X.Q. Wang. *Phys. Rev. B* **74**, 165308 (2006)

5. H. Kallel. *Phys. Rev. B* **86**, 085318 (2012)

6. J. Walentin; *Science* **339**, 1057 (2013)

7. R. Yan, D. Gargas and P. Yang. *Nat. Photon.* **3** 569-576 (2009)

8. B. Loitsch, D. Rudolph, S. Morktter, M. Dblinger, G. Grimaldi, L. Hanschke, S. Matich, E. Parzinger, U. Wurstbauer, G. Abstreiter, J.J. Finley and G. Koblmller. *Advanced Materials* **27** 2195-2202 (2015)

9. M. Law, D.J. Sirbuly, J.C. Johnson, J. Goldberger, R.J. Saykally and P. Yang. *Science* **305** 1269-1273 (2004)

10. L. Cao, P. Fan, A.P. Vasudev, J.S. White, Z. Yu, W. Cai, J.A. Schuller, S. Fan and M.L. Brongersma. *Nano Letters* **10** 439-445 (2010)

11. R. Ruppin. *J. Opt. Soc. Am. A* **15** 1891-1895 (1998)

12. L. Cao, P. Fan, E.S. Barnard, A.M. Brown and M.L. Brongersma. *Nano Letters* **10** 2649-2654 (2010)

13. J.A. Schuller, R. Zia, T. Taubner and M.L. Brongersma. *Phys. Rev. Lett.* **99**(10) 107401 (2007)

14. T. Nobis, E.M. Kaidashev, A. Rahm, M. Lorenz and M. Grundmann. *Phys. Rev. Lett.* **93**(10) 103903 (2004)

15. D. van Dam, D.R. Abujetas, R. Paniagua-Domínguez, J.A. Sánchez-Gil, E.P.A.M. Bakkers, J.E.M. Haverkort and J.G. Rivas. *Nano Letters* **15** 4557-4563 (2015)

16. F.J. Lopez, J.K. Hyun, U. Givan, I.S. Kim, A.L. Holsteen and L.J. Lauhon *Nano Letters* **12** 2266-2271 (2012)

17. Q. Xiong, G. Chen, H. Gutierrez and P. Eklund. *Applied Physics A* **85** 299-305 (2006)

18. G.S. Doerk, C. Carraro and R. Maboudian. *Raman spectroscopy for characterization of semiconducting nanowires Raman Spectroscopy for Nanomaterials Characterization* (Springer) pp 477-506 (2012)

19. L. Cao, B. Nabet and J.E. Spanier. *Phys. Rev. Lett.* **96**(15) 157402 (2006)

20. A. Torres, A. Martín-Martín, O. Martínez, A.C. Prieto, V. Hortelano, J. Jiménez, A. Rodríguez, J. Sangrador and T. Rodríguez. *Applied Physics Letters* **96** 011904 (2010)

21. L.J. Lauhon, M.S. Gudiksen, D. Wang and C.M. Lieber. *Nature* **420** 57-61 (2002)

22. T.S. Le, P. Jannaty, X. Luo, A. Zaslavsky, D.E. Perea, S.A. Dayeh and S.T. Picraux. *Nano Letters* **12** 5850-5855 (2012)

3. Objectives

The aim of this work is the study of the interaction between light and heterostructured semiconductor NWs. For this, micro-Raman spectroscopy is used as a local probe of the local electromagnetic field inside the NW. Since the Raman signal produced by a volume of material is proportional to the local intensity of the excitation light, i.e. the square of the electric field modulus $|E|^2$, a series of micro-Raman measurements can provide information about the distribution of the EM field inside the NWs. This becomes especially relevant when dealing with heterostructured NWs, systems with localized interphases where interesting physical processes are expected to occur.

On the other hand, the light-NW interaction is not well understood at this time, being currently under study. In this framework, this work aims to the development of a model that allows to improve the understanding of light-matter interaction at the nanoscale, and to explain the new optical phenomena occurring in subwavelength nanostructures, namely NWs. For this purpose, we will use finite element methods (FEM) to solve numerically the Maxwell equations for the EM field inside the NW in order to study the light/ NW interaction, aiming to interpret the experimental data.

4. State of the Art

4.1.Raman Spectroscopy

Raman spectroscopy is widely used as an optical characterization tool for investigating semiconductors in bulk, thin film, nanostructured, and device forms[1-10]. When light interacts with a solid, three main phenomena take place: reflection, absorption and light scattering. The light scattering can be either elastic (Rayleigh) when the scattered light frequency (energy) is unaltered, or inelastic otherwise. The Raman effect is an inelastic scattering phenomenon in which phonons, the quasi-particles associated to the elementary excitations of the solid, are either created or absorbed by the incident electromagnetic wave. Since lattice vibrations are very sensitive to the local structure and lattice environment, the Raman spectrum supplies information about the physical factors that disturb the local order or modify the interatomic distances. A great number of fundamental properties of semiconductors can be studied by Raman spectroscopy, i.e., crystal orientation, lattice temperature, symmetry breakdown, strain, chemical composition, among others; moreover, electronic and thermal properties can also be probed. Raman spectroscopy emerges as a valuable tool for device development and diagnosis, which is today used as a routine tool in the microelectronics industry, in particular, for the assessment of local stresses in microelectronic devices[11-13], but also, for the local lattice temperature assessment in devices under operation[14-16]. The variety of information provided by Raman spectroscopy combined with the slightly sub-micrometric spatial resolution of the optical microscopy, the relative experimental simplicity, and its non-invasive character, make of it an essential tool for the characterization of semiconductors and devices.

The Raman effect consists of the coupling of the electromagnetic field of the incident light with the optical phonons through the induced electric dipole moment. The energy exchange between the incident light and the solid can take place in two different ways. The first one is the excitation of a lattice vibration by the incident light, with the subsequent loss of energy, this is called the Stokes (S) Raman scattering. The second one is the absorption of a lattice vibration by the incident light, with the corresponding increase of the light energy, this is the Anti-Stokes (AS) Raman scattering. In both processes the energy transfer is always that of the absorbed/emitted phonon according to the energy conservation law, then, these two mechanisms appear in the Raman spectrum as symmetric peaks with respect to the Rayleigh radiation,

and the difference with respect to the Rayleigh (incident) energy directly informs us about the phonon energy, see Fig. 4.1. Typical phonon energies (≈ 10-100 meV) are normally very small as compared to the IR-visible-UV photon energies (> 1eV); as a result, first order Raman peaks are very close to the Rayleigh radiation, which is several orders of magnitude more intense than the Raman signal. Therefore, a Raman spectrometer does need a very efficient laser beam cut-off system. For this purpose, either notch, or edge filters are used, which allow to simplify the spectrometers, improving their luminosity, which is crucial for Raman spectroscopy applications.

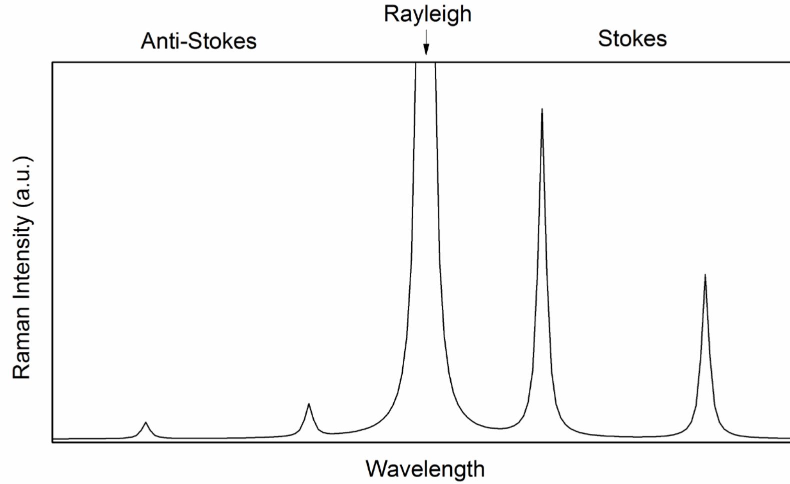

Figure 4.1 Typical Raman spectrum showing the differences between Stokes and Anti-Stokes bands, and their positions with respect to the Rayleigh scattering.

The energy and momentum conservation rules for first-order Raman scattering (one phonon processes) are

$$\hbar\omega_i \pm \hbar\omega_{ph} = \hbar\omega_s \quad ; \quad \vec{k}_i \pm \vec{q} = \vec{k}_s \tag{4.1}$$

where ω refers to the angular frequency and k to the wavevector of incident (subscript i) and scattered (subscript s) photons respectively, and ω_{ph} and q are the angular frequency and wavevector of the phonon involved in the scattering process. The plus sign applies to the AS component and the minus sign refers to the S scattering.

In the visible range, in which the Raman excitation is usually done, $\omega_i \ll \omega_{ph}$, which means that $\vec{k}_i \cong \vec{k}_s \cong \vec{k}$, which is of the order of 10^4-10^5 cm^{-1}. The maximum value of q (q_{max}) of the Brillouin zone is about 10^8 cm^{-1}, 3-4 orders of magnitude higher

than the wavevector of the visible light. For a typical backscattering Raman experiment excited with photons of wavelength λ in the visible range, and a material with refractive index n, the maximum value of q is given by $q_{max} = 4\pi n/\lambda$ which results in values around 10^6 cm^{-1} for materials with high refractive index such as semiconductors (n ~ 4). This should mean that only phonons of the zone center are allowed by the momentum conservation law and can be seen in the first-order Raman spectrum. The breakdown of the lattice symmetry relaxes the momentum selection rules allowing scattering with the participation of phonons of the full Brillouin zone. This will represent a crucial issue for the study of semiconductor nanostructures, where the size limitation breaks the translational symmetry of the bulk material, and the existence of the surface can even induce novel effects such as surface phonons. According to this, semiconductor nanostructures constitute, nowadays, one of the most relevant application cases of the Raman spectroscopy[21, 22].

Since Raman scattering is a second-order optical process, it should contain a great deal of symmetry information as compared to a first-order optical processes. The symmetry selection rules are easily explained in the frame of a semiclassical description of the Raman effect (for the quantum mechanics approach see Ref. 23). The electric field, $\vec{E}(\omega_i) = \vec{E}_0 e^{i\omega_i t}$, of the incident electromagnetic wave induces a dipole moment in the solid:

$$\vec{P}(\omega_s) = \varepsilon_0 \chi \vec{E}(\omega_i) \tag{4.2}$$

where χ is the generalized dielectric susceptibility tensor, which can be expanded as a function of the normal coordinates of the atoms in the lattice, u_j. Then the polarization adopts the following expression[3]:

$$\vec{P}(\omega_s) = \varepsilon_0 \chi^{(0)} \vec{E}_0(\omega_i) e^{i\omega_i t} + \varepsilon_0 \chi_j^{(1)} u_j \vec{E}_0(\omega_i) e^{i(\omega_i \pm \omega_{ph})t} + ... \tag{4.3}$$

The first term of the expansion corresponds to the Rayleigh scattering (unaltered frequency). The second one corresponds to the first order Raman scattering, it depends on $\chi^{(1)}$, the first derivatives of the susceptibility with respect to the atomic displacements u_j (eigenmodes associated to the corresponding vibration), and involves only one phonon. The following terms correspond to second order Raman scattering, which involves two phonons, followed by the successive higher orders processes involving several phonons that will not be discussed here.

The differential Raman scattering cross section for Stokes scattering can be calculated from the polarization to be[1]:

$$\frac{d\sigma}{d\Omega} = V\omega_s^4|\vec{e}_i \cdot R \cdot \vec{e}_s|^2(n+1) \tag{4.4}$$

where $\vec{e}_i$ and $\vec{e}_s$ are the polarization vectors of the incident and scattered light, V the sampled volume and R is the Raman tensor, which is proportional to $\chi^{(1)}$. For Anti-Stokes scattering the formula is identical but replacing $(n+1)$ by n, and ω_S by ω_{AS}. n is the phonon population, that follows the Bose-Einstein distribution

$$n = \frac{1}{exp\left(\frac{\hbar\omega}{kT}\right) - 1} \tag{4.5}$$

In order to have a non-zero scattering cross section the factor $|\vec{e}_i \cdot R \cdot \vec{e}_s|$ must be different from zero, and this is determined by the crystal point group symmetry, information contained in R, and the polarization of the incident and scattered light beams, given by $\vec{e}_i$ and $\vec{e}_s$. This set of conditions are known as the Raman symmetry selection rules[23] and they explain the presence or absence of the different Raman peaks depending on the experimental geometrical configuration. On the other hand, the scattering cross section is needed for the calculation of the Raman intensity

$$I \propto \sigma I_0 \propto V\omega^4 E_0^2 \tag{4.6}$$

I_0 is the excitation laser intensity, which is proportional to the square of its electric field. In brief, Raman intensity is proportional to the sampled volume, to the fourth power of the excitation light frequency, and to the value of the square of the electric field.

It is important to note that S radiation is always more intense than AS radiation, because AS scattering needs the existence of a lattice vibration to be absorbed by the incident light, making it a much less suitable process from an statistical point of view. The probability of an AS event taking place will strongly depend on the temperature of the solid, since higher temperatures result in higher number of excited lattice vibrations, which means a higher phonon population n. This can be easily seen in the equation for the scattering cross section: S scattering has a factor $(n+1)$, while AS scattering is only proportional to n; at room temperature the phonon population is $n \sim 10^{-2} \ll 1$. Usually, Raman experiments deal with the S

component, because its intensity is several times higher than that of the AS component, ~ 50 times at room temperature. Moreover, the ratio between S and AS intensities allows to perform contact-less temperature measurements together with the Raman spectroscopy, according with the following equation

$$\frac{I_S}{I_{AS}} \propto \frac{n+1}{n} = exp\left(\frac{\hbar\omega}{kT}\right) \tag{4.7}$$

The thermal aspects are crucial in nanostructures, where the thermal conductivity, and heat dissipation are dramatically affected by the low dimensionality;[17] e.g. Si nanowires immersed in low heat dissipation media present evident signs of overheating in the presence of a laser beam for the acquisition of the Raman spectrum[18-20].

4.2. Carrier dynamics in semiconductor NWs

The properties of low dimensional systems substantially differ from those of their bulk counterparts[24,25]. One of the key factors affecting the behavior of these systems is the surface condition, according to their high aspect ratio. When the solid state theory is used to study bulk material properties, the first assumption is the solid to be infinite, i.e. having no surface. It is a good approximation whenever the surface/volume ratio is small enough. However, low dimensional structures have surfaces by definition, limiting the system and modifying its properties in an important way, as well as increasing the surface/volume ratio.

In a bulk material the carrier recombination takes place by two different ways: band to band recombination and trap assisted recombination. These recombination processes can be grouped in a single carrier lifetime, τ_{bulk}. However, in a low dimensional system, the presence of the surface provides surface states for electrons and holes, creating parallel recombination paths with its corresponding lifetime τ_{surf}. The main effect of the surface recombination is the reduction of the effective carrier lifetime, increasing the recombination rate and lowering the carrier density. According to this, the carrier recombination dynamics can be established as follows:

$$\left(\frac{\partial n}{\partial t}\right)_{rec} = \frac{\Delta n}{\tau_{bulk}} + \frac{\Delta n}{\tau_{surf}} = \frac{\Delta n}{\tau_{eff}} \tag{4.8}$$

where Δn are the excess carriers. The surface recombination lifetime of a low dimensional system can be calculated from its reduced length, called l, and the surface recombination velocity (SRV), S. For a 1D system, the reduced length is the NW radius, and thus the surface lifetime can be expressed as a function of the NW diameter, d.[26]

$$\frac{1}{\tau_{surf}} = \frac{2S}{l} = \frac{4S}{d} \tag{4.9}$$

When the semiconductor NW is under illumination electron-hole pairs are created, giving a carrier generation term, G, which depends on the illumination intensity, wavelength, and the semiconductor properties. This term should be taken into account when studying the global carrier dynamics. When the NW is under illumination, photogenerated carriers will recombine until equilibrium is reached, then the total carrier density at equilibrium should not change

$$\frac{dn}{dt} = \left(\frac{\partial n}{\partial t}\right)_{gen} - \left(\frac{\partial n}{\partial t}\right)_{rec} = G - \left(\frac{1}{\tau_{bulk}} + \frac{1}{\tau_{surf}}\right)\Delta n = 0 \tag{4.10}$$

This condition allows the computation of the excess carriers

$$\Delta n = \frac{G}{\left(\frac{1}{\tau_{bulk}} + \frac{4S}{d}\right)} \tag{4.11}$$

The major factor that affects the SRV is the surface quality. Typical crystalline Si NWs grown by VLS method, as the ones used in this work, present a native oxide layer at the surface, being the quality of this oxide layer what determines the number of recombination centers, and thus the SRV. Therefore, modifying the surface properties changes the SRV, and consequently the equilibrium free carrier density.[26-28]

The presence of free carriers will modify the NW electric conductivity, according to the following equation

$$\sigma = en\mu_n + ep\mu_p \tag{4.12}$$

which shows a direct relation between carrier densities, n and p, and conductivity σ, being μ_n and μ_p the mobilities of electrons and holes, respectively. On the other hand, the electric conductivity directly affects the electromagnetic response of the NW by

increasing the dielectric losses. This effect is contained in the imaginary part of the relative electric susceptibility

$$\varepsilon = \varepsilon' - i\varepsilon'' \quad \rightarrow \quad \varepsilon'' = \varepsilon_0'' + \frac{\sigma}{\varepsilon_0 \omega} \tag{4.13}$$

Then, a higher electric conductivity yields higher dielectric losses. At the same time, the presence of dielectric losses affects the distribution of the EM field, lowering the field intensity when the dielectric losses increase, and then the Raman signal.

As a summary, the Raman signal is sensitive to the carrier density, which varies with the surface quality. If the contribution of the free carriers is taken into account a change in the Raman signal should be detected when the surface state is modified. This effect give us the perfect tool to check the effect of the free carriers on the Raman signal of semiconductor NWs.

4.3. Finite Element Method

Finite Element Methods (FEM) were originally developed for solving solid mechanics problems[29,30]. The original problem starts with a solid with known mechanical properties and satisfying certain boundary conditions. If an external force is applied on the solid, what are the values of the displacements, stresses and strains at each point of the solid? This problem consists of 15 equations, 9 of them partial differential equations, making it impossible to find an exact solution. In 1909 Ritz developed a method to find an approximate solution to this problem[31], this method was improved along the last century and became the FEM that we use nowadays.

First of all let us remember how numerical integration works. When we have a function that cannot be integrated analytically, we divide the interval of integration in small sections, then the function is approximated in each section by another simpler function: constant, linear, quadratic, etc. Since this functions can be easily integrated in each section, and the integral operation is linear, an approximation to the integral can be computed as a linear combination of different values of this simpler functions at certain points. The idea for FEM is essentially the same. In a first step the solid is divided in a set of small pieces creating a mesh, then a simple function is used to approximate the problem function in each piece. The values of the function in the nodes of the mesh are used as unknowns, and the partial differential equations for the

original function along with the boundary conditions become a set of linear equations for the unknowns, which are much easily solvable. This set of linear equations is derived from a variational formulation, by minimizing a suitable error function. FEM have been widely used in science, mainly in applied physics: elasticity, fluid dynamics, heat transfer, etc., but also in fundamental physics: non-linear optics, electromagnetic (EM) fields, waveguides design, etc.

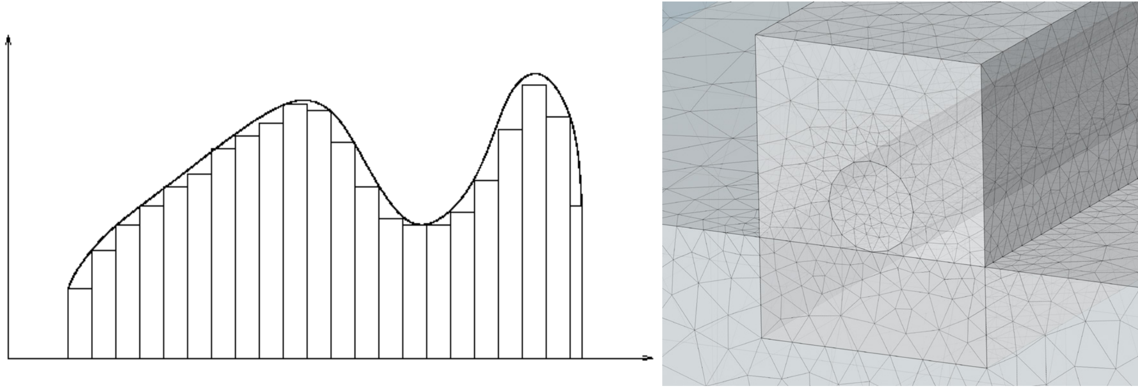

Figure 4.2 Left: Numerical integration of a curve using the rectangle rule. Right: 3D mesh used in a FEM calculation of the EM field in the interior of a semiconductor NW.

From Raman Scattering theory it is known that the Raman signal generated in a certain volume of material is proportional to the square of the electric field (see Section 3.1). According to this, FEM has been used in this work to simulate the laser/NW interaction by solving the Maxwell equations in the presence of the NW and its environment. The solution of the problem provides the distribution of the electromagnetic field, which allow us to calculate the theoretical Raman signal.

Typically, these calculations for homogeneous and core-shell heterostructured NWs were carried out by means of the Lorenz-Mie theory, which is the theoretical solution of the process of light scattering by an infinitely long dielectric cylinder immersed in a homogeneous and isotropic non absorbing medium.[32] In the frame of this formalism, the calculation of the absorption and scattering efficiencies, Q_{abs} and Q_{sc} respectively, has revealed a strong dependence of these coefficients with the NW diameter, presenting resonances for certain diameters.[33,34] Alternatively, we analyzed the NW/laser beam interaction by solving the equivalent 2D Maxwell equations using the radio-frequency (RF) module of the COMSOL Multiphysics simulation software, contrasting our results with the solution of the Lorentz-Mie equations and obtaining an excellent agreement.[35] In this kind of problem the symmetry along the NWs axis allows for the simplification of the problem to a 2D one, by studying the section of the

NW perpendicular to its axis. However, because of symmetry-breaking, the simulation of the axially heterostructured NWs cannot be performed by a 2D approach like the one typically used when studying the light/NW interaction for homogeneous and core-shell heterostructured NWs.[36,37] Thus we have proceeded to solve a 3D model, which is necessary to account for the axial HJ and the finite length of the NW; these two features break the symmetry of the longitudinal dimension and make it impossible to reduce the system to a 2D problem. We built a full 3D electromagnetic model for a HJ NW with the same characteristics as the ones used in the experiments, placed on a metallic substrate (Al) and surrounded by air. The air/NW/substrate system was limited by Cartesian perfectly matched layers (PMLs), which absorb all the outgoing radiation, eliminating secondary reflections on the boundaries.

The laser beam in our model is described as a focused Gaussian beam, instead of the usual approach, both in 2D simulations and Mie theory, of considering a plane wave. That could be a good approximation for certain experiments with a uniform illumination; however when doing micro-Raman measurements, the excitation laser beam is focused in a small region where the spot size is comparable to the size of the NW. In this situation, the distribution of the EM field inside the NW is far away from that induced by a homogeneous illumination, and the plane wave approximation is not accurate.

The equations for the field of a Gaussian laser beam propagating along the z axis are the following[36-38]:

$$E_x(r,z,t) = E_0 \frac{w_0}{w(z)} e^{\left(\frac{-r^2}{w^2(z)}\right)} e^{\left(ik\frac{r^2}{2R(z)}\right)} e^{i(kz-\omega t)} e^{i\zeta(z)} \tag{4.14}$$

$$w(z) = w(0)\sqrt{1+\left(\frac{z\lambda}{\pi w_0^2}\right)} \quad ; \quad R(z) = z\left(1+\left(\frac{\pi w_0^2}{z\lambda}\right)^2\right)$$
$$\zeta(z) = \arctan\left(\frac{z\lambda}{\pi w_0^2}\right) \tag{4.15}$$

where cylindrical coordinates are used, r is the distance to the beam axis (z axis), and z is the position with respect to the focal plane ($z = 0$). $R(z)$ is the radius of curvature of the wavefront at z, $\zeta(z)$ is called the Gouy phase at z, typical of Gaussian and

spherical wavefronts, $w(z)$ is the diameter of the Gaussian spot at z which depends on its value at the focus $w_0 = w(0)$, the so called waist size.

The waist size is determined from the laser wavelength and the NA of the objective (0.95 in this case) by the Abbe's formula

$$w_0 \propto \frac{1{,}22\lambda}{NA} \tag{4.16}$$

The magnetic field can be derived from the electric field by using the Maxwell equation for the curl of the electric field

$$\nabla \times \vec{E}(r,z) = -i\omega\mu\vec{H}(r,z) \tag{4.17}$$

Once the excitation laser beam and the system have been modelled, the FEM software solves the equations of the scattered field. The scattered field is defined as the EM field generated by the system when the excitation beam, E_b, is applied, in order to create a total EM field satisfying the Maxwell equations

$$\vec{E}_{tot} = \vec{E}_b + \vec{E}_{sc} \quad \leftrightarrow \quad \vec{E}_{sc} = \vec{E}_{tot} - \vec{E}_b \tag{4.18}$$

The mathematical treatment is quite similar to that of perturbation theory, since E_b is known from the beginning, it is the laser beam EM field.

When the distribution of the total EM field inside the NW is known the expected Raman signal of each segment of the NW can be calculated. The Raman signal emitted by a small volume of the material is proportional to the square of the electric field modulus, $|E|^2$; therefore, once we have calculated the distribution of the electric field, the total Raman signal produced by a certain region of the NW will be proportional to the integral of $|E|^2$ over the corresponding volume. By computing these integrals we can know the theoretical intensity of the signal emitted by each region of the NW.

Finally, the model is solved for different positions of the laser beam along the NW axis in order to reproduce the experimental measurements of a longitudinal profile over a NW, calculating the Raman intensities of each NW region as a function of the laser beam position.

References

1. *Light Scattering in Solids, Topics in applied Physics.* M. Cardona, G. Guntherodt, Springer Verlag, Heildelberg , vols. 8, 50, 51, 54, 66, 68.

2. P. Bruesch. *Phonons: Theory and Experiments I*; Springer series in Solid State Sciences, vol. 34; ed. by M. Cardona, P. Fulde, and H.J. Queisser (Springer, Berlin 1982).

3. F.H. Pollak. *Analytical Raman Spectroscopy.* Chem. Anal. Ser. 114, J. Grasseli, B.J. Bulkin Editors (J. Wiley, N.York 1991).

4. W. Richter; *Resonant Raman Scattering in Semiconductors*, Springer Tracts in Modern Physics 78, ed. by G. Hohler (Springer, Berlin 1976).

5. G. Abstreiter, E. Bauser, A. Fischer, K. Ploog. *Appl. Phys. A* **16**, 345 (1978).

6. B. Prevot, J. Wagner; *Prog. Crystal Growth, Charact.* **22**, 245 (1991).

7. I. Zardo, G. Abstreiter, A. Fontcuberta. *Raman Spectroscopy on Semiconductor Nanowires*, Nanowires, Paola Prete Editor, ISBN: 978-953-7619-79-4, (InTech, Rijeka 2010).

8. R.L. McCreery. *Raman Spectroscopy for Chemical Analysis.* Monographs of Analytical Chemistry and its applications, J.D.Winefordner Editor; Vol 57 (J. Wiley, New York, 2000).

9. *Handbook of Raman Spectroscopy: From the Research Laboratory to the Process Line.* ed. Ian R. Lewis. G.M. Edwards, (Marcel dekker, 2001).

10. *Raman Spectroscopy for Nanomaterials Characterization.* C.S.S.R. Kumar Editor (Springer Verlag, Berlin-Heidelberg 2012).

11. I. De Wolf. *J.Raman Spectrosc.* **30**, 87 (1999).

12. I. De Wolf, H.E. Maes, S.K. Jones; *J.Appl. Phys.* **79**, 7148 (1996).

13. T. Tada, V. Poborchii, T. Kanayama; *J.Appl. Phys.* **107**, 113539 (2010).

14. S. Todoraki, *J. Appl. Phys.* **60**, 61 (1986).

15. H. Brugger, P.W. Epperlein, S. Beeck and G. Abstreiter, *Inst. Phys. Conf. Ser.* **106**, 771 (1990).

16. A. Sarua, A. Bullen, M. Haynes, M. Kuball. *IEEE Trans Electron. Devices* **54**, 1838 (2007).

17. D.G. Cahill, W.K. Ford, K.E. Goodson, G.D. Mahan, A. Majumdar, H.J. Maris, R. Merlin, S.R. Phillpot. *J.Appl. Phys.* **93**, 793 (2003).

18. A. Torres, A. Martín-Martín, O. Martínez, A.C. Prieto, V. Hortelano, J. Jiménez, A. Rodríguez, J. Sangrador, T. Rodríguez. *Appl. Phys. Lett* **96**, 011904 (2010).

19. R. Jallilian, G.U. Sumanasekera, H. Chandrasekharan, M.K. Sunkara. *Phys. Rev. B* **74**, 155421(2006).

20. H. Scheel, S. Reich, A.C. Ferrari, M. Cantoro, A. Colli, C. Thomsen. *Appl. Phys. Lett.* **88**, 233114 (2006).

21. W. Richter, Z.P. Wang, L. Ley. *Solid State Commun.* **39**, 625 (1981).

22. H. Campbell, P.M. Fauchet. *Solid State Commun.* **58**, 739 (1986).

23. W. Hayes, R. Loudon; Light Scattering in Solids (J.Wiley, New York 1978).

24. M. Law; *Annu. Rev. Mater. Res.* **34**, 83 (2004).

25. R. N. Musin and X.Q. Wang; *Phys. Rev. B* **74**, 165308 (2006).

26. Y. Dan, K. Seo, K.Takei, J.H. Meza, A. Javey, and K.B. Crozier; *Nano Lett.* **11**, 2527-2532 (2011).

27. O. Demichel et al. *Nano Lett.* **10**, 2323-2329 (2010).

28. A.J. Sabba and D.M. Riffe. *J. Appl. Phys.* **88(**11) 6954-6956 (2000).

29. K.J. Bathe and E.L. Wilson. *Numerical Methods in Finite Element Analysis.* Prentice-Hall, Inc. (1976).

30. *The finite element methods: Linear static and dynamic finite element analysis.* T.J.R. Hughes. Dover Publications (1987).

31. W. Ritz. *J. Reine Angew. Math.* **135**, 1-61 (1909).

32. G. Brönstrup, N. Jahr, C. Leiterer, A. Csáki, W. Fritzsche and S. Christiansen. *ACS Nano* **4**, 7113-7122 (2000).

33. J. Anaya, J. Jimenez, A. Rodriguez and T. Rodríguez. *MRS Proceedings* **1627**, mrsf13-1627-l09-38 (2014).

34. F.J Lopez, J.K. Hyun, U. Givan, I.S. Kim, A.L. Holsteen and L.J. Lauhon. *Nano Lett.* **12**, 2266-2271 (2012).

35. Q. Xiong, G. Chen, H. Gutierrez and P. Eklund. *Applied Physics A* **85**, 299-305 (2006).

36. O. Svelto, D. David, C. Hanna. *Principles of lasers*, 5th edition, Springer, Heilderberg (2010).

37. B.E.A. Saleh, M.C. Teich. *Fundamentals of Photonics* Ch. 5, John Wiley & Sons, (1991).

38. M.V. Berry. *J. Opt. A: Pure Appl. Opt.* **6**, 475 (2004).

5. Experimental

5.1. Sample Preparation

The samples used in the first part of this work are $Si_{1-x}Ge_x$/Si (SiGe/Si) HJ NWs, and pure Si NWs. These NWs were grown by the vapour-liquid-solid (VLS) method using a commercial low pressure chemical vapour deposition (LPCVD) reactor. Si_2H_6 and GeH_4 were used as precursor gases and alloyed Au-Ga metal droplets were used as catalysts. These NWs where grown by the group of T. Rodríguez and A. Rodríguez.[1,2] Single Si NWs were grown at 470 ºC using Si_2H_6 as a precursor; while the simple HJ SiGe/Si NWs (with a Ge atomic fraction close to 0.1) were grown at 430 ºC using GeH_4 and Si_2H_6 gas precursors; the carrier gas was H_2, preserving for the different precursor flow ratios a total pressure of 400 mTorr all over the growth run. Under these growth conditions straight NWs with uniform diameters ranging from 20 to 100 nm were obtained depending on the metallic droplet diameter. Heterostructured SiGe/Si NWs were grown initially as homogeneous SiGe NWs, and at a certain point the GeH_4 source is switched off, while keeping a continuous flow of Si_2H_6. This provides a phase transition from SiGe to Si, and then the desired heterostructured NWs.

In the last experimental measurements double HJ NWs were used. Double HJ NWs with the structure SiGe/Si/SiGe were grown by the group of Thierry Baron.[3] The growing mechanism was also VLS, and the procedure is similar. The first SiGe segment grows up to a certain point when the source of Ge, GeH_4, is switched off. The Ge concentration in the droplet falls and the Si segment starts growing. In a second step, the Ge source is switched on again, in order to grow the last SiGe segment. A more detailed explanation of the growing parameters, and also a complete study of these heterostructured NWs can be found in Ref. 3.

In VLS growth the abruptness of the HJ depends on the solubility of the atomic species in the catalyst metal. Due to the reservoir effect in the catalyst droplet, once the precursor gas source (GeH_4) is switched-off, the remaining atoms dissolved in the catalyst droplet produce a compositionally graded trailing junction, starting at the composition of the homogeneous SiGe segment, and goes to zero, forming a compositionally graded interface between the two NW segments. This effect is particularly relevant in the Si-Ge system because of the high solubility of Ge in Au. This means that the HJ presents a characteristic SiGe/Si trailing profile with a HJ width roughly equivalent to the NW diameter.[3-5] A possible way to control the

abruptness of the HJ is the use of catalyst droplets with different Si and Ge solubilities, for example Au-Ga alloys. The presence of Ga in the alloy reduces the solubility of both Si and Ge, resulting in a more sudden HJ transition. According to this we will work with three kind of samples, depending on the catalyst droplet used during the growth: in the first batch pure gold nanoparticles were used, labeled as 100; in the second one the alloy is $Au_{0.9}Ga_{0.1}$, labelled as 90; and for the third one $Au_{0.5}Ga_{0.5}$ was used, labelled as 50. As a result, the HJ width is reduced with increasing Ga concentration in the droplet.

For the sample preparation, the as grown NWs were separated from the substrate in an ultrasonic bath, and suspended in methanol. A droplet of this suspension is spread out on an Al substrate, which has been proved to improve the Raman signal.[6] In the first place the presence of a metallic surface enhances the Raman signal simply by reflecting both the excitation laser beam and the scattered Raman light. Secondly, the contact between the NW and the metallic surface allows heat dissipation directly through the metal, which is more efficient than convection through air. This improves the thermal management of the laser induced heating, with respect to free standing NWs, avoiding a thermal shift of the Raman signal, and the subsequent misunderstanding of the experimental results.

Prior to the Raman measurements the NWs morphology and their environment are studied by scanning electron microscopy (SEM). If we want good and reliable Raman measurements it is crucial to find isolated NWs with a clean environment. Firstly, the absence of foreign particles ensures a "clean" Raman spectrum, with Raman radiation coming only from the NW. Secondly, the composition of the NW varies along its axis, then the measurement method will consist of a longitudinal series of Raman spectra, recorded every 100 nm along the NW axis. This permits to easily locate the NW ends, where the signal falls off, and the presence of the HJ when the spectrum changes dramatically. The presence of other NWs in the vicinity of the one being studied could interfere with the measurement if they are close enough.

The Raman spectra have been recorded with a high resolution Labram UV-HR 800 Raman spectrometer from Horiba-Jovin Yvon. The excitation and the scattered light collection were performed by means of a confocal metallographic microscope with a high magnification objective (100X and 0.95 numerical aperture (NA)). The excitation was done with a frequency doubled Nd:YAG laser (532 nm). The parameters of the spectrometer have been fixed for all experiments: room temperature is 20 ºC,

the pinhole diameter is 300 μm and a D0.6 filter is used to reduce the incident laser intensity to 142 μW. The intensity has been selected to produce a maximum Raman signal without laser induced heating. Finally, the spectrometer diffraction grating, with 2400 lines per millimeter, has been chosen to achieve a maximum spectral resolution, better than 0.5 cm^{-1}. Regarding the integration times, i.e. the exposition time to take one spectrum, 30 s are enough to get a good signal, albeit 60 s measurements provide cleaner spectra and the required time is affordable. So the vast majority of the measurements have been performed with an integration time of 60 s.

5.2. Simple Heterojunction NWs

As it has been explained in the Raman spectroscopy section (section 3.1) the Raman signal is proportional to the excitation volume. When measuring single NWs the excitation volume is small, so the expected signal will also be low, and we should be very careful in order to obtain good Raman measurements.

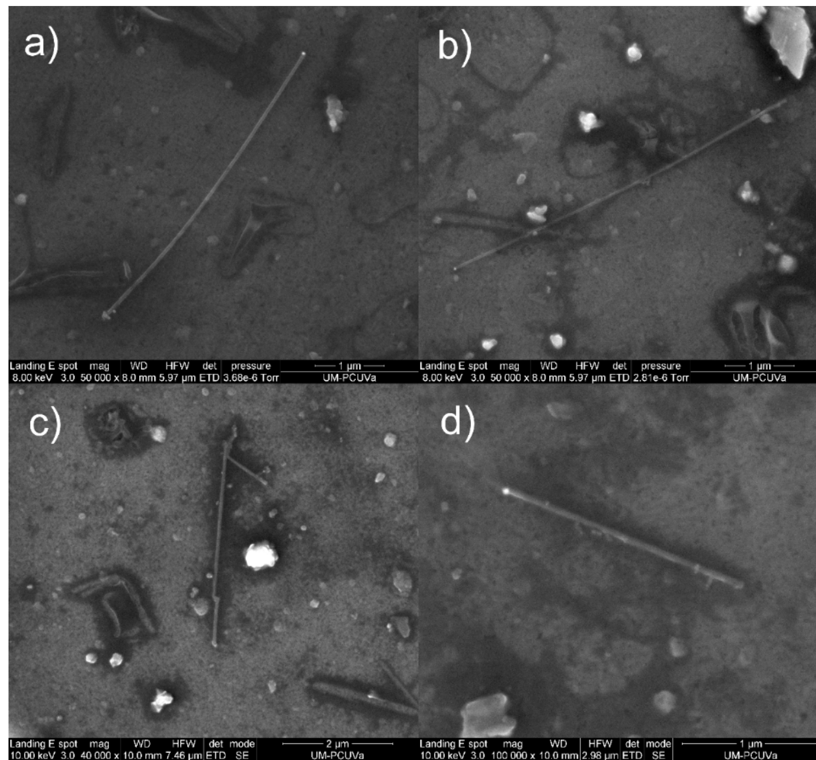

Figure 5.1 SEM images of NWs grown with $Au_{0.5}Ga_{0.5}$ droplets. a) 51: a clean NW suitable for Raman measurements. b) 52: there are small NWs in the region, and also foreign particles. c) 54: a broken NW, also with other NWs in touch. d) 55: a NW surrounded by little NWs next to it, moreover it does not present SiGe phase. b, c and d are not suitable for Raman measurements.

In Fig. 5.1 four different NWs of the group 50 ($Au_{0.5}Ga_{0.5}$ droplets) are presented. We can see how the NW 51 (Fig. 5.1a) is clean and straight, suitable for a reliable measurement. However the other three NWs in Fig. 5.1, b, c and d, are not in a clean environment, or present growth defects.

The first Raman measurements were performed on a NW of the 90 group ($Au_{0.9}Ga_{0.1}$ droplets), labelled as 92, with a diameter around 40 nm. Fig. 5.2 shows four Raman spectra recorded in different positions along this NW. On the right side, a SEM image with the acquisition regions of the four Raman spectra is provided.

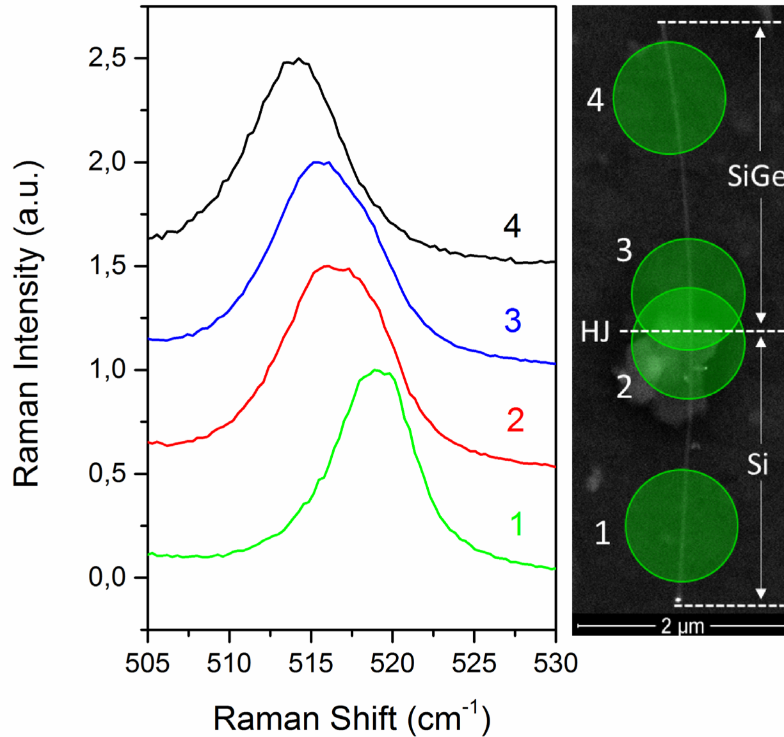

Figure 5.2 Raman spectra at 4 specific points along NW 92. The SEM image shows the acquisition region of each spectrum. There are clear differences between the two spectra in the homogeneous segments, 1 and 4, and the spectra of the HJ region, 2 and 3. The last ones are broader and highly asymmetric.

The spectra 1 and 4 were recorded in the homogeneous segments of both Si and SiGe, respectively. The position of the peak in the Si segment corresponds to the Si-Si vibration in pure Si, located at 520.6 cm^{-1}. The position of the peak in the SiGe segment corresponds to the Si-Si vibration in the SiGe alloy, which is shifted to a lower wavenumber because of the presence of Ge, for simplicity we will label it as SiGe since

it comes from the SiGe segment. The position of this peak, ~514 cm^{-1}, informs us about the Ge composition. Using the following formula[7]

$$\omega_{Si}(x) = 520.0 - 68\ x \quad \rightarrow \quad x = \frac{520.0 - \omega_{Si}}{68} \tag{5.1}$$

the Ge composition has been found to be around 0.1, in good agreement with energy dispersive X-Ray (EDX) spectroscopy measurements in a transmission electron microscope (TEM). Spectra 2 and 3 were recorded in two different points with the laser beam illuminating partially the two pure segments as well as the HJ. When these spectra are compared with the others, a dramatic change is observed in the spectral shape of 2 and 3 with respect to 1 and 4. Spectra 1 and 4 show typical Lorentzian-shape peaks, with the spectral parameters characteristic of Si and $Si_{90}Ge_{10}$ respectively.[8,9] Meanwhile, the spectra recorded in positions 2 and 3 appear broadened and asymmetric, as a consequence of the overlapping contribution to the Raman spectra of the different regions of the NW being simultaneously excited by the laser beam. Therefore, in order to analyze this signal, a spectral deconvolution shall be carried out to ascertain the different contributions of the different NW regions.

For the deconvolution we use the spectra recorded in the homogeneous segments, like spectra 1 and 4 of Fig. 5.2, as the references for the fitting. However, trying to accomplish a satisfactory fit with just two spectra is not possible. Even if the convolution is not a simple averaged sum of the two peaks, but a full convolution weighted by the Gaussian profile of the laser spot, the experimental spectra cannot be properly fitted. The best result that we obtained by using the only contribution of the two homogeneous segments is shown in the inset of Fig. 5.3.

As a result of the spectral separation between the peaks of the two homogeneous segments, it is impossible to combine the two peaks to form a single one, but the valley located in the middle keeps them separated, regardless of their proportion in the convolution. The experimental measurements of the HJ region can only be fitted properly if a third peak is added, see Fig. 5.3. The third peak parameters, position and width, are left as free parameters during the fit; while the parameters of the other two peaks are fixed, because they are known from the spectra of the homogeneous segments. The position and width of this third peak, calculated through the best fit of the data, are always intermediate between these of Si and $Si_{0.9}Ge_{0.1}$, as a result we conclude that

this signal could only come from a region with intermediate properties between those of the homogeneous segments, which is precisely the HJ region.

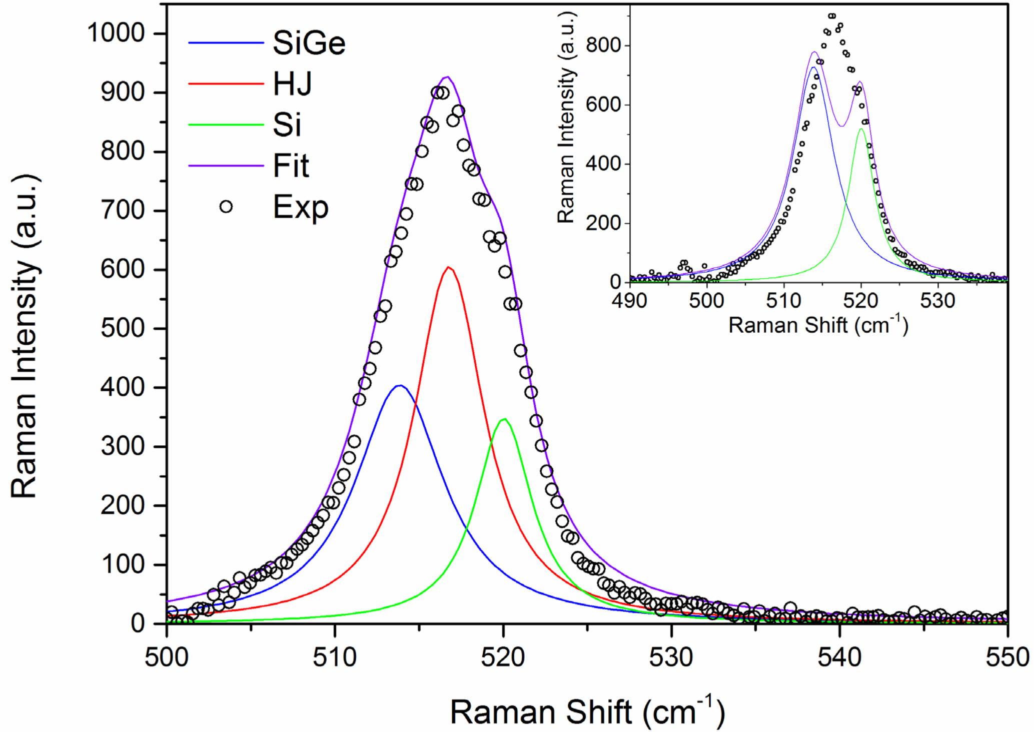

Figure 5.3 Fit of one of the experimental spectra of the HJ region of NW 92. A satisfactory fit is only achieved with three Raman bands. The inset shows the "best" fit that can be obtained with the use of only two bands.

The question now is if this result is coherent. As it has been explained in the Raman Spectroscopy section, the intensity of the Raman signal is proportional to the scattering volume. The width of the HJ region of a NW grown by VLS method is roughly equivalent to the NW diameter, ~40-50 nm in this case, because of the Ge reservoir effect on the catalyst droplet. On the other hand, the width of the illuminated region of the homogeneous segments when the laser beam is centered at the HJ should be roughly half of the laser spot diameter, ~450-500 nm. Then, the geometrical scattering volume of the HJ is ~10X smaller than that of the illuminated regions of the homogeneous segments. If we try to reproduce the experimental measurements according to the scattering volume of every region we should get a signal coming from the HJ 10X smaller than that of the homogeneous segments. However, as we can see in Fig. 5.3 the intensities of all the Raman bands are comparable (in this case the HJ signal is even higher). As a result, the effective scattering of the HJ region should have been enhanced with respect to the scattering due to its geometrical volume, resulting

in an amplification phenomenon related to the HJ itself. The amplification factor depends on the studied NW, and it has been found to be in a range between 8X to 12X depending on the studied NWs.

We have shown that the experimental Raman spectra cannot be explained through the only contribution of the two homogeneous segments, neither if we consider the HJ region with its geometrical volume. In order to explain the measurements we need to consider the signal coming from the HJ and also an amplification factor of around 10X.

The other experimental observation that points to an amplification effect is the measurement of a longitudinal scan along the NW axis. In such kind of measurements, Raman spectra are recorded every 100 nm along the NW axis. Then, each spectrum is fitted following the same procedure of the spectrum in Fig. 5.3, taking as a reference the spectra of the homogeneous segments. This mathematical treatment gives us the intensities of the three Raman peaks arising from the probed zones of the NW: Si segment, SiGe segment and HJ. When the treatment is performed for all the spectra of the longitudinal scan, the total Raman signal and the contribution of each segment can be plotted as a function of the laser beam position. With this we can easily see the position of the NW ends, the homogeneous segments and the location of the HJ. In Fig. 5.4 we present the longitudinal scan of the NW 51 (shown in Fig. 5.1), with a diameter of around 44 nm.

It is clear that the Raman signal of the three regions are comparable again, highlighting the local amplification of the small volume of the HJ. Moreover, the total Raman signal also presents a maximum when the laser beam is crossing the HJ, evidencing that the presence of the HJ is enhancing the overall Raman intensity, and thus affecting the distribution of the electric field inside the NW. It should be noted that this amplification behavior of the total Raman signal was observed for all of the several axially heterostructured NWs that we have studied.

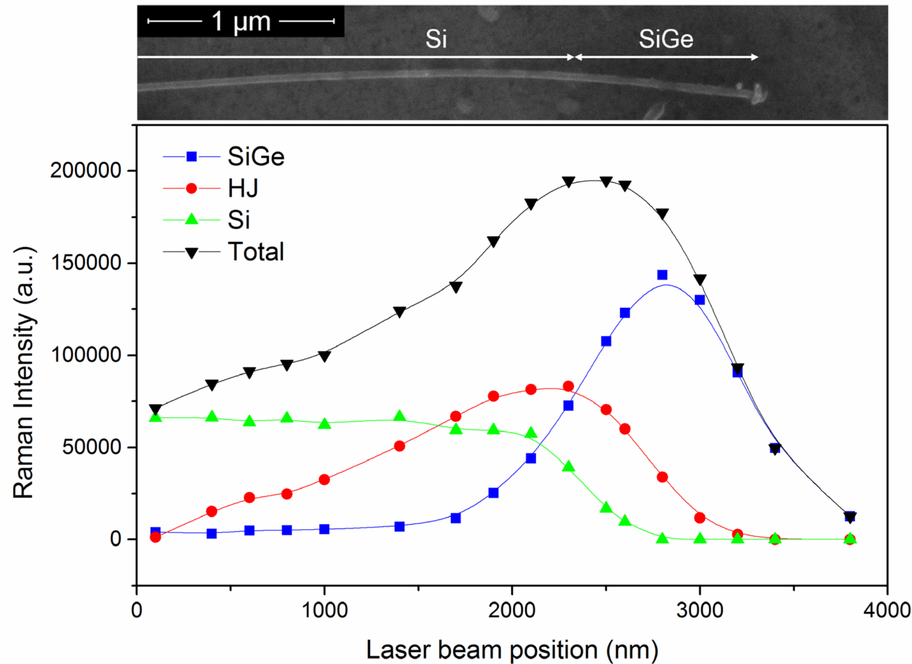

Figure 5.4 Longitudinal scan along the NW 51, showing the amplification of the total Raman signal around the HJ region. Also the contribution of each NW region, Si, SiGe and HJ, is presented. The plot data continues homogeneously on the left side up to the end of the Si segment.

Regarding the dependence of the results with the composition of the catalyst droplets we can say that no clear correlation has been observed. It is mainly due to the difficulty of finding a great number of NWs which are suitable for a good measurement. To obtain a confident result we would need a series of NWs with exactly the same diameter and coming from different catalyst droplets. However, the NWs diameters follow a continuous distribution and it is really difficult to find NWs with a predefined diameter.

5.3. Double Heterojunction NWs

In order to ensure the existence of the amplification effect that was observed in the first experiments new NWs, with different properties, are needed. In particular we were looking for NWs with more Ge concentration, because the Si-Si peak shift increases with Ge concentration. If the separation of the peaks is higher both the resolution and the spectral deconvolution process will be highly improved. Moreover, when the Ge concentration is high enough two new Raman peaks can be detected: one

associated to the Ge-Ge vibration, located around 300 cm^{-1}, and another one associated to the Si-Ge vibration, around 400 cm^{-1}. Note that the frequencies of these peaks depend on the alloy composition. The presence of more peaks makes the amplification effect more clear, and also helps to separate the signals coming from the different regions.

The studied NWs are double heterojunction NWs, formed by three segments and two different phase transitions, following the structure SiGe/Si/SiGe. According to the growth method, the first HJ presents the typical trailing profile for the Ge composition because of the catalyst droplet reservoir effect, it is exactly the same situation as that of the simple HJ NWs mentioned above. Nevertheless, the second HJ presents a leading profile, much more abrupt since the Ge is immediately solved in the catalyst when the source is switched on again, and starts its deposition in the new segment. For more details about these NWs structure and growth process see Sample Preparation section and its references.

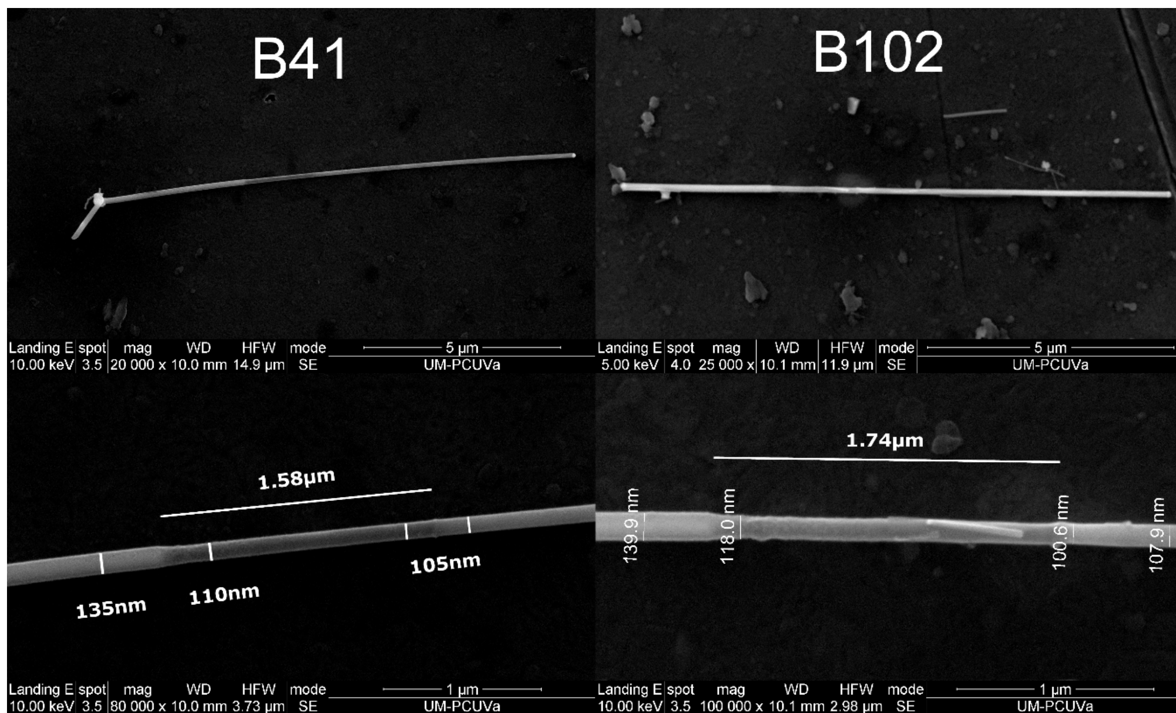

Figure 5.5 SEM images of two different double HJ NWs: left B41, right B102. The lower images show a zoom of the interesting region of each double HJ NW. In both images the trailing HJ is on the left of the Si segment, and the leading HJ on the right (the Au droplet is always on the right end of the NW).

Figure 5.5 shows SEM images of the two studied NWs: B41 and B102. It can be seen how the two HJs, trailing and leading, are morphologically different. The diameters and length of the Si segment are similar for both NWs. As we did with the simple HJ NWs we performed a longitudinal scan along the two NWs, so we can locate the NW ends, the different segments, and the HJs. The results are presented in Figures 5.6, 5.7 and 5.8.

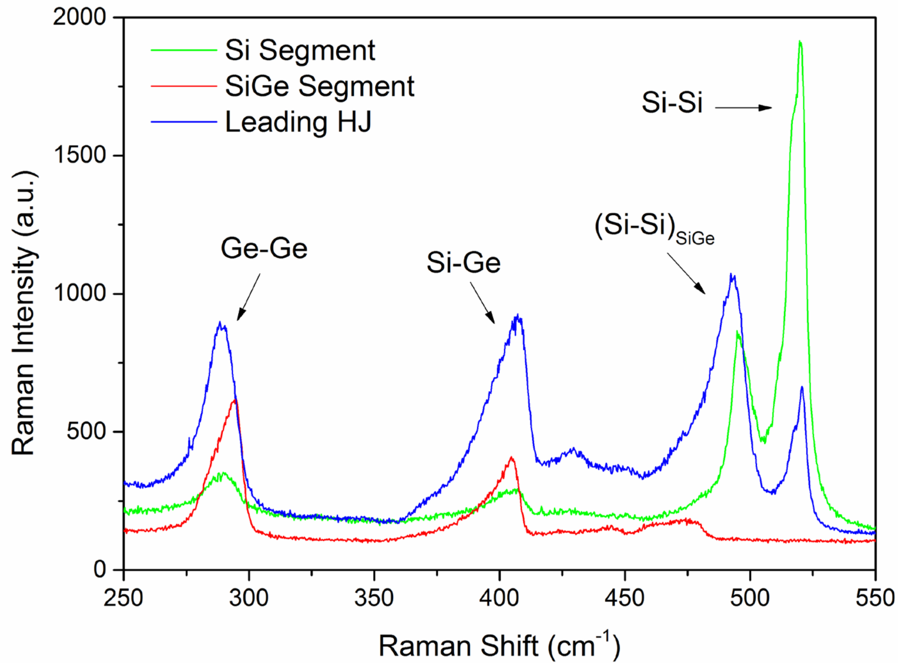

Figure 5.6 Representative Raman spectra of each of region of the double HJ NW B41. The three Raman peaks of the SiGe alloy are pointed out, remarking the shift of the Si-Si vibration in the SiGe alloy.

Fig. 5.6 shows three typical Raman spectra recorded in three key regions of the double HJ NW B41: the SiGe segment, the Si segment and the leading HJ. We see that the SiGe spectrum shows a very little contribution of the Si-Si peak, this tell us that the Ge composition of the homogeneous segments is quite high. From the relative intensity of the Ge-Ge and Si-Ge peaks we can estimate it to be around 0.6-0.7, however, no EDX measurements have been performed yet. On the other hand, the spectrum of the Si segment shows also little contribution of the other two peaks. Since it is known that the Si segment is formed by pure Si this signal should come from the adjacent SiGe segments. This can be easily understood due to the short length of the Si segment, according to the Gaussian distribution even when the laser spot is centered

in the Si segment the laser beam will be exciting the SiGe. Finally, the spectrum of the leading HJ region presents all those contributions.

Once the longitudinal profiles of both NWs, B41 and B102, are recorded, each spectrum, like the ones shown in Fig. 5.6, undergoes a deconvolution process to deduce the contribution of each peak. Figures 5.7 and 5.8 represent a plot of this contributions as a function of the laser beam position along the NW axis.

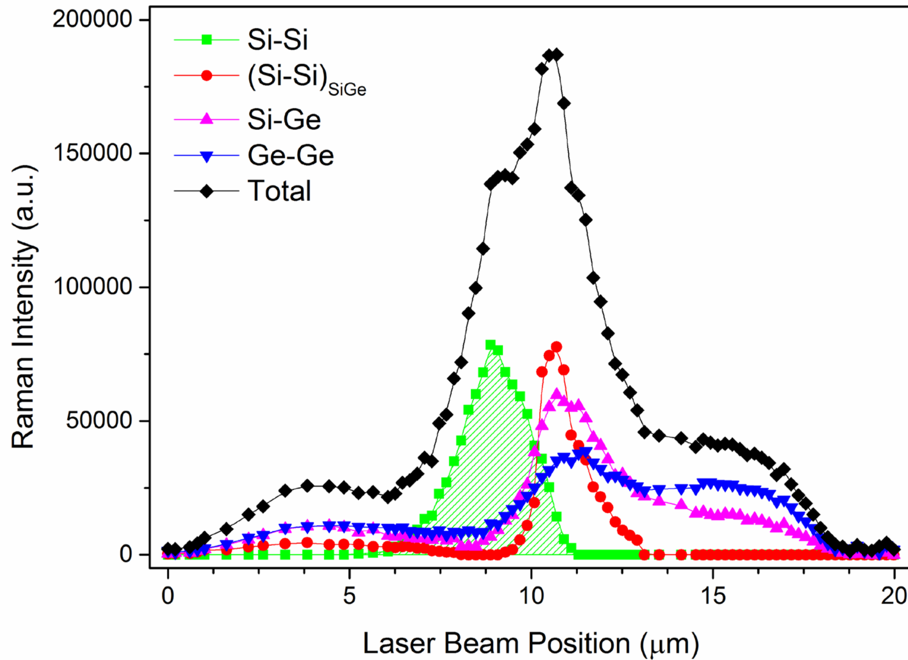

Figure 5.7 Longitudinal scan along the NW B41. The area under the Si-Si curve informs about the location of the pure Si segment. A clear amplification is observed in the signals coming from the HJ, $(Si\text{-}Si)_{SiGe}$ and Si-Ge, also in the total Raman signal and slightly in the Ge-Ge peak. This amplification only takes place in the leading HJ.

Both Figures 5.7 and 5.8 show similar profiles, in both cases we can clearly see the presence of the amplification at the HJ region. We see also that even though the signal of the Si segment is higher than that of the SiGe segments, the maximum always coincides with the HJ and not with the Si segment, highlighting again the presence of the amplification effect at the HJ. Surprisingly, the amplification does only appear in one of the HJs, actually in the leading one. We do not have a final explanation for this observation, but we have in mind some interesting hypothesis, and we think that this discrepancy between both HJs could be an interesting clue for the understanding of the underlying physics of this effect. The main difference between both HJs is the width, i.e. the abruptness, being the leading HJ much sharper than the trailing one.

Another important difference can be seen in the SEM images of the double HJ NWs, Fig. 5.5, the leading HJ shows a diameter larger that the adjacent segments, which in the image looks like a ring around the interphase region. This ring is not present in the trailing HJ, but a continuous transition from SiGe to Si is observed, with a mild decrease in diameter.

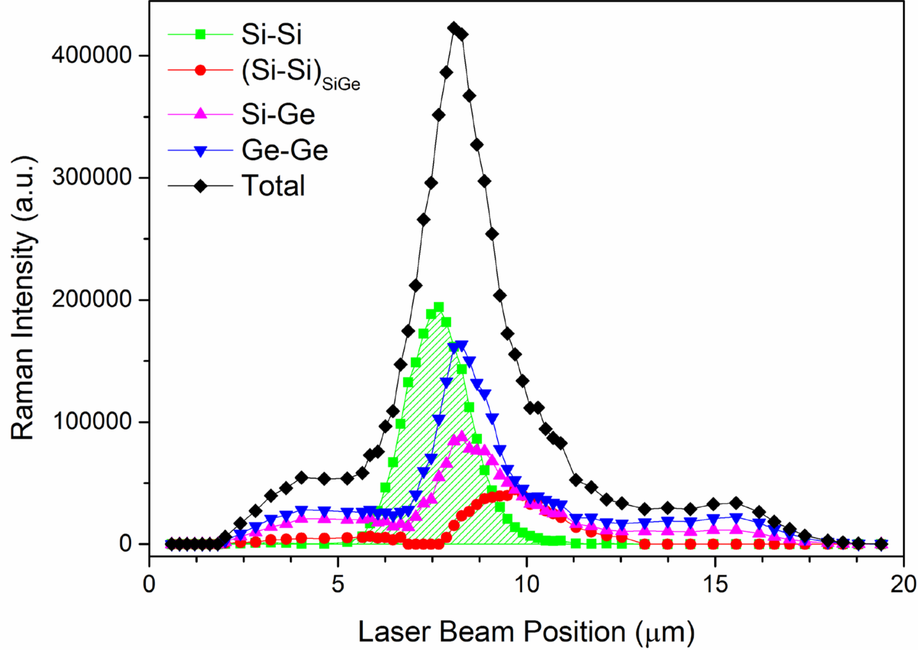

Figure 5.8 Longitudinal scan of the NW B102. The amplification is observed again, however the presence of the parasitic NW in this area makes the data not fully reliable. In any case the amplification process only takes place in the leading HJ again.

We have checked the amplification effect in NWs with different structure, and also different composition. The amplification effect takes place again in the HJ region, however it only appears in one of the two HJs. The proper understanding of the opposite behavior of both HJs could be the key point to unveil the physics under the amplification effect.

5.4. Chemical Passivation of the NWs Surface

In this last part of the experimental results we will check the presence of photogenerated free carriers by taking advantage of the carrier dynamics, which are controlled by the surface recombination at the nanoscale. In order to do this we will modify the surface condition to reduce the surface recombination velocity, and thus inducing a change in the free carrier density. In this situation we will check if the Raman signal varies as the model predicts.

The experiment will start with the chemical etching of pure Si NWs with a HF solution (≈4%). Si NWs are preferred to HJ NWs for simplicity in the data manipulation, for the homogeneity of the chemical attack, since the Si NW surface is homogeneous, and because of the ease of its manufacture with respect to heterostructured NWs. The chemical treatment removes the SiO_2 external layer and does not react with the crystalline Si core, leaving a clean Si NW with a hydrogen terminated surface.[10-12] If our hypothesis of the presence of free carriers is correct, immediately after the removal of the oxide layer surface recombination states will be nearly suppressed, then the equilibrium carrier density will raise, lowering the Raman signal. As time goes on and the spontaneous oxidation process takes place, new recombination centers are created at the surface and carrier density decreases, with the concomitant increment of the Raman signal.

Our sample consists of Si NWs grown over a crystalline Si substrate by VLS. The sample is dipped in a 4% HF solution for 20 minutes and then dried in a flowing N_2 atmosphere to avoid oxidation. The NWs are suspended in methanol in a sonication bath, and deposited in the Al substrate (see Sample Preparation). NWs are kept in N_2 atmosphere during the evaporation of the methanol up to the first Raman measurement. After this point the N_2 source is switched off and the oxidation process starts at room temperature. We continuously recorded longitudinal scans along the NW axis. This method is preferred to single spectra since slight variations of the position can modify substantially the spectrum, with this measurement the NW ends are used as a reference. The mean Raman signal of a single Si NW along two days of measurements can be seen in Fig. 5.9.

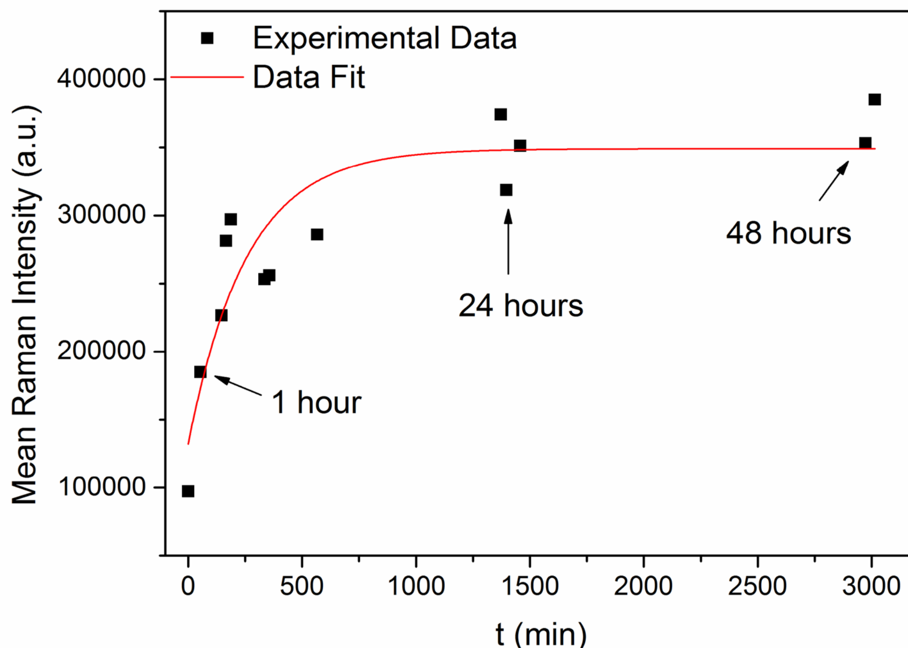

Figure 5.9 Evolution of the mean Raman Intensity of a clean Si NW as a function of the oxidation time. The intensity becomes stable around 25-30 hours after the oxidation beginning, which coincides with the formation of the first stable oxide layer.[10]

The whole experience lasted for one week of measurements, albeit the Raman signal became fully stable after 2 days of oxidation. We can see also that the intensity is starting to reach the stable value after the first 24 hours. This is in good agreement with the time needed for the formation of the first stable oxide layer in Si at room temperature, which lies around 25-30 hours.[10] It should be noted that the Raman signal raises rather fast in the first hours of oxidation. This suggests that the creation of a full oxide layer is not needed to enhance the surface recombination, but the creation of sparse defects at the surface is enough to spoil the homogeneity of the Si surface, and create surface states. With the presence of recombination centers at the surface, the equilibrium free carriers decrease and the Raman signal is progressively recovered.

References

1. A. Rodríguez, J. Sangrador, T. Rodríguez, C. Ballesteros , A. C. Prieto, J. Jiménez. *MRS Symp.Proc.* **1258**, P05-05 (2010).

2. A. Rodríguez, T. Rodríguez, C. Ballesteros, J. Jiménez. *MRS Symp. Proc.* **1510**, DD06-05 (2013).

3. P. Periwal, N.V. Sibirev, G. Patriarche, B. Salem, F. Bassani, V.G. Dubrovskii, T. Baron. *Nano Lett.* **14**, 5140 (2014).

4. D.E. Perea, N. Li, R.M. Dickerson, A. Misra, S.T. Picraux. *Nano Lett.* **11**, 3117 (2011).

5. T.E. Clark, P. Nimmatoori, K.K. Lew, L. Pan, J.M. Redwing, E.C. Dickey, *Nano Lett.* **8**, 1246 (2008).

6. J. Anaya, A. Torres, A.C. Prieto, V. Hortelano, J. Jiménez, A. Rodríguez, T. Rodríguez. *Appl. Phys. A* **114**, 1321-1331 (2014).

7. J.C. Tsang, P.M. Mooney, F. Dacol, and J.O. Chu. *J. Appl. Phys.* **75**, 12, (1994).

8. M.I. Alonso and K. Winer. *Phys. Rev. B* **39**(14) 10056-10062 (1989).

9. T.P. Pearsall. *Critical Reviews in Solid State and Materials Sciences*, **15** 551-600 (1989).

10. M. Morita et al. *J. Appl. Phys.* **68** (3), 1272-1281 (1990).

11. M. Grundner and H. Jacob, *Appl. Phys. A* **39**, 73 (1986).

12. B.S. Swain, B.P. Swain, N.M. Hwang. *Current Applied Physics* **10**, S439-S442, (2010).

6. Simulations

Along this chapter we will explain the results obtained from a physical model of the laser/NW interaction, which will be solved using the FEM software COMSOL Multiphysics, as depicted in the State of the Art. The first and simplest model of the electromagnetic interaction will show qualitatively the effect of localization and amplification of the EM field. However, the quantitative results does not match the experimental amplification. In a second step the model will be improved to fully explain the experimental results.

In a first step the response of a perfectly dielectric NW was calculated. This model was solved for different positions of the excitation laser beam along the NW axis in order to reproduce the experimental profile of NW 51, Fig. 5.4. A particular solution of the model is shown in Fig. 6.1, showing a representation of the model, with the 3D distribution of the relative intensity of the electric field. The relative intensity of the electric field is defined as $E_r^2 = |E|^2/|E_{incident}|^2$, i.e. the local electric field enhancement over the incident laser electromagnetic field. In the same figure we also included the profile of this magnitude along the NW axis, highlighting the local enhancement at the HJ region.

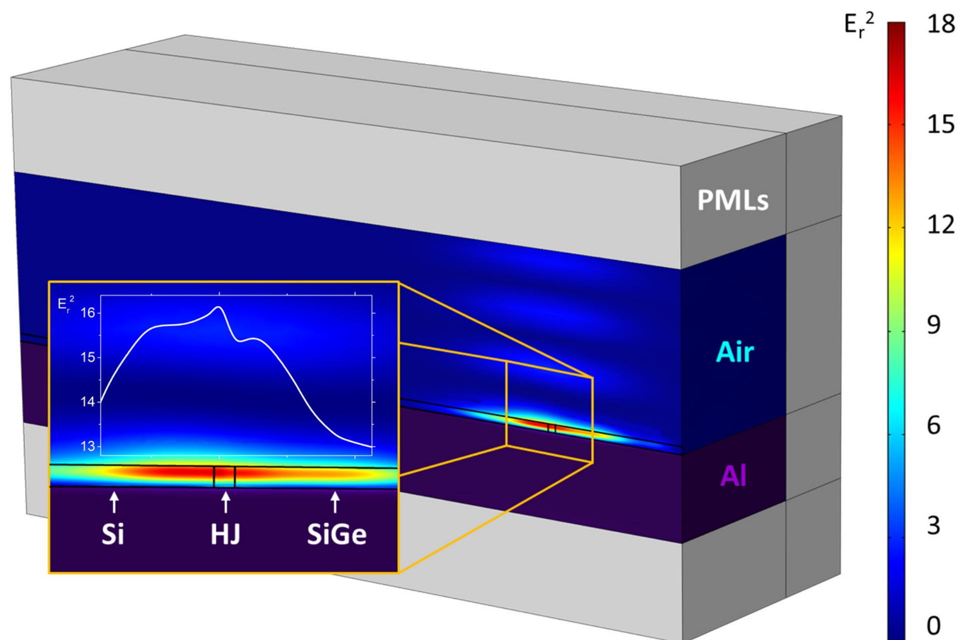

Figure 6.1 3D distribution of the relative electric field intensity, E_r^2, in a dielectric HJ NW. The enlarged image shows de profile of E_r^2 along the NW axis, highlighting the local enhancement at the HJ region.

For each position of the laser beam the electromagnetic field distribution inside the NW is calculated. The volume integrals of the square of the electric field modulus, $|E|^2$, in the three different regions: Si segment, SiGe segment and the HJ, are then calculated. The value of these integrals should be proportional to the theoretical Raman signal arising from each NW region under the excitation beam (see Raman Scattering theory, section 3.1). Despite this model is showing an amplification and localization of the EM field in the HJ region, the calculated amplification is one order of magnitude lower than the one deduced from the experimental data, Fig. 6.2.

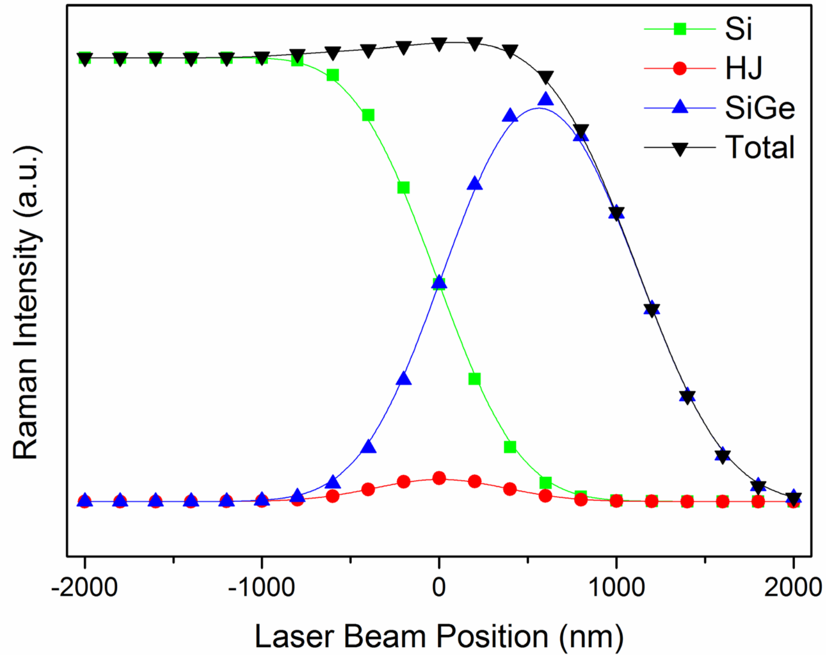

Figure 6.2 Simulated longitudinal scan of a dielectric NW with the same characteristics of NW 51 (see Fig. 5.4). The model predicts a slight amplification that does not match the experimental one.

In order to explain this discrepancy, a more complete model accounting for the effect of the free carriers, either photogenerated or native, was considered. It should be noted that the presence of free carriers will contribute to the dielectric losses, as explained. For the excitation conditions of our measurements and a surface recombination velocity (SRV) of $S \sim 3\ 10^5$ cm/s, it results in a photogenerated carrier concentration of $n \sim 10^{19}$ cm^{-3}, in good agreement with other experimental estimations.[1,2] As it has been explained, the dielectric losses will mainly affect the regions with free carriers, i.e. the two NW segments; but as a consequence of the carrier depletion at the HJ, this region will be free of the losses associated with the presence

of free carriers. Therefore, the dielectric losses will modify the electric field distribution inside the NW, lowering the electric field in the homogeneous segments, which contain free carriers, with respect to the carrier depleted HJ, which yields an effective amplification of the HJ signal.

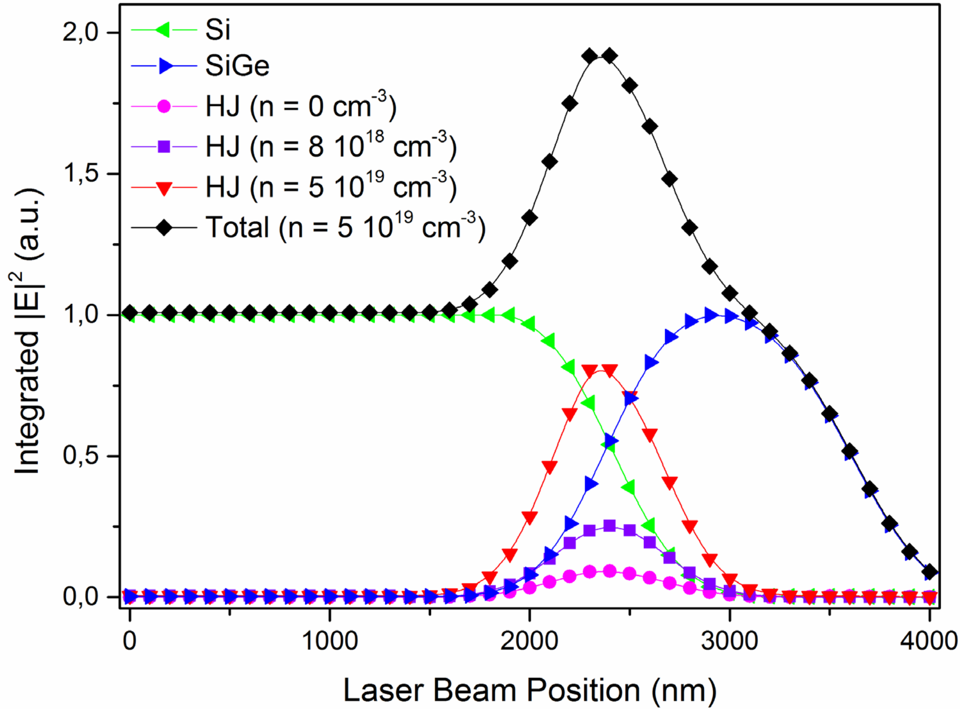

Figure 6.3 Simulated longitudinal scan of the NW 51 for different free carrier concentrations. The curve of the total Raman signal (Total) corresponds to the higher carrier concentration, which better reproduces the experimental results of Fig. 5.4.

Once the free carriers were considered the model was solved for two different carrier densities: $n = 8\ 10^{18}$ cm^{-3} and $n = 5\ 10^{19}$ cm^{-3}. The results are shown in Fig. 6.3. From these results it appears clear that including the free carriers, photogenerated in this case, in the expected range of 10^{18}-10^{20} cm^{-3} results in a contribution of the narrow HJ region similar to the one observed in Fig. 5.4. However, it should be noted that the predictions from the model show some differences with the experimental Raman intensities (Fig. 5.4). In particular the experimental intensity of the SiGe segment is higher than the intensity measured for the Si segment, as opposed to the EM-FEM model which shows similar values for both segments. This difference might arise due to a difference of a few nanometers in the diameter of both segments, in fact diameter changes in the presence of axial HJs are quite common. Because of the diameter dependent resonance, a subtle diameter change can be responsible for the observed

difference in the Raman intensity. The results of Fig. 6.3 were calculated for an ideal cylindrical NW, without diameter change, and then no relevant difference is observed.

The full EM-FEM simulation reveals that the observed enhancement of the local electric field at the HJ arises from the laser/HJ electromagnetic coupling, explaining the presence of the third band in the Raman spectra of the HJ region, and confirming the enhancement of the local electric field at the HJ.

References

1. Y. Dan, K. Seo, K.Takei, J.H. Meza, A. Javey, and K.B. Crozier; *Nano Lett.* **11**, 2527-2532 (2011).

2. A.J. Sabba and D.M. Riffe. *J. Appl. Phys.* **88(**11) 6954-6956 (2000).

7. Conclusions and Future Work

We have presented along this work an electromagnetic amplification phenomenon in the HJ region of axially heterostructured SiGe/Si NWs when interacting with a laser beam. This nanoscale effect has been systematically studied by recording the Raman signals of the heterostructured NWs, which show a significant enhancement at the HJ region with respect to those obtained in compositionally homogeneous NWs of the same dimensions. The Raman signal of the HJ region of several NWs presents an intensity per unit volume around 10 times higher than the NW pure segments. In order to check the existence of this amplification other NWs with different composition and structure were measured, namely double HJ NWs. The amplification is observed again, and even more clearly because of the higher Ge concentration, which permits the analysis of the three Raman bands of SiGe. However, the amplification is only observed in the leading type HJ, and no amplification appear in the trailing one. We do not have a definitive answer for this difference, albeit we deal with several hypothesis. Nevertheless, more research around this unexpected feature is needed since it could provide key information to fully understand the amplification effect.

The experimental observations were contrasted with the results obtained by the 3D solution of the Maxwell equations for the interaction between the dielectric NW and the focused laser beam using an EM-FEM model. The model accounts for the above experimental observations, and shows the possibility of locally modify the electric field in the heterojunction; however, the calculated electric field enhancement at the HJ is lower than the one observed experimentally in the Raman spectra. A further improvement of the model considering the contribution of free carriers improves the calculated values up to the experimental observations. The effect of free carriers on the Raman signal was tested in a new experiment. Pure Si NWs underwent a chemical etching process to remove their native oxide layer, as a result surface recombination is suppressed and carrier density raises, lowering the Raman signal. The experimental results matched perfectly the prediction of the theory, initially showing a weak Raman signal that progressively recovers as the NW surface is oxidized.

The future work in the short term will be the exhaustive investigation of the double HJ NWs, especially the behavior difference of the two HJs. Also new single HJ NWs with higher Ge concentration are recently available and will be studied. For

medium/long term work we are planning to add electrical contacts to some NWs and investigate their electrical properties. Moreover, it will be interesting to analyze the electro-optical response by illuminating the NWs at different points and recording the induced electric current. The electro-optical characterization is an essential step to explore the possible applications of axially heterostructured NWs for optoelectronic devices.

Part of the results of this memory were presented in EXMATEC 2016, Aveiro (Portugal), and are the object of a publication submitted to Nanotechnology.